

# Palladium Mesowire Arrays for Fast Hydrogen Sensors and Hydrogen-Actuated Switches

E. C. Walter,<sup>†</sup> F. Favier,<sup>‡</sup> and R. M. Penner<sup>\*,†</sup>

Department of Chemistry, University of California, Irvine, California 92679-2025, and UMR 5072, CNRS-UMII, 34095 Montpellier, France

**Arrays of mesoscopic palladium wires prepared by electrodeposition form the basis for hydrogen sensors and hydrogen-actuated switches that exhibit a response time ranging from 20 ms to 5 s, depending on the hydrogen concentration. These devices were constructed by electrodepositing palladium mesowires on a highly oriented pyrolytic graphite surface and then transferring these mesowires to a cyanoacrylate film supported on a glass slide. The application of silver contacts to the ends of 10–100 mesowires, arrayed electrically in parallel, produced sensors and switches that exhibited a high conductivity state in the presence of hydrogen and a low conductivity state in the absence of hydrogen. After an initial exposure to hydrogen, 15–50 nanoscopic gaps are formed in each mesowire. These nanoscopic gaps or “break junctions” close in the presence of hydrogen gas and reopen in its absence as hydrogen is reversibly occluded by the palladium grains in each wire, and the palladium lattice expands and contracts by several percent. The change in resistance for sensors and switches was related to the hydrogen concentration over a range from 1 to 10%.**

Hydrogen is an extremely clean energy source for use in fuel cells and internal combustion engines.<sup>1–3</sup> However, widespread use of hydrogen as a fuel will require innovations in hydrogen storage and hydrogen sensing. Reliable, cheap, compact, and safe H<sub>2</sub> sensors are needed both for measuring the hydrogen concentration in flowing gas streams and for monitoring ambient air for leaked hydrogen. It is essential that “alarm” sensors detect H<sub>2</sub> at a concentration well below the lower explosion limit in air of 4%.

The vast majority of hydrogen sensors use a palladium element to selectively absorb hydrogen.<sup>4</sup> Such sensors operate by detecting a change in the properties of the palladium/hydrogen solution relative to those of pure palladium. The properties detected include mass,<sup>5,6</sup> volume,<sup>7–9</sup> electrical resistivity,<sup>10–15</sup> optical constants,<sup>16–22</sup>

and the work function.<sup>23–27</sup> Palladium-based hydrogen sensors have two main problems: First, the response time for these devices, ranging from several minutes to 0.5 s, is too slow to permit useful, real-time monitoring of flowing gas streams. Second, palladium is poisoned by exposure to reactive species that chemisorb on the palladium surface and block adsorption sites needed for H<sub>2</sub>, such as hydrocarbons, O<sub>2</sub>, H<sub>2</sub>O, and CO.<sup>4</sup> These species are exactly the sorts of contaminants that are likely to be present in the gaseous feed stream supplying a fuel cell or an internal combustion engine. Exposure of a palladium-based hydrogen sensor to these gases causes the response time for the sensor to increase, and can necessitate recalibration of the sensor for hydrogen.

The response time for a palladium-based H<sub>2</sub> sensor is determined by the rate at which the palladium (Pd) element equilibrates with H<sub>2</sub> in the contacting gas phase. Equilibration of pure palladium with a hydrogen-containing carrier gas involves the fast dissociative adsorption of H<sub>2</sub> at the palladium surface and the subsequent diffusion of hydrogen atoms into the palladium lattice. Since the diffusion coefficient for hydrogen atoms in palladium is  $\sim 10^{-7}$  cm<sup>2</sup> s<sup>-1</sup>,<sup>28</sup> this process, not the dissociation chemisorption

\* To whom correspondence should be addressed. rmpenner@uci.edu.

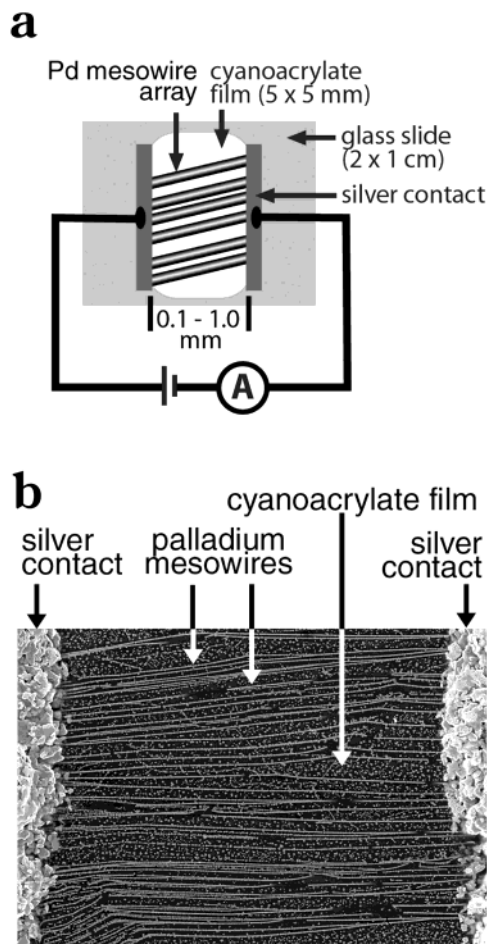
<sup>†</sup> University of California, Irvine.

<sup>‡</sup> CNRS-UMII.

- (1) VanBlarigan, P.; Keller, J. O. *Int. J. Hydrogen Energy* **1998**, *23*, 603–609.
- (2) Peschka, W. *Int. J. Hydrogen Energy* **1998**, *23*, 27–43.
- (3) North, D. C. *Int. J. Hydrogen Energy* **1992**, *17*, 509–512.
- (4) Christofides, C.; Mandelis, A. *J. Appl. Phys.* **1991**, *68*, R1.
- (5) Bucur, R. V.; Mecca, V.; Flanagan, T. B. *Surf. Sci.* **1976**, *54*, 477.
- (6) Franzer, G. A.; Glosser, R. J. *Phys. D: Appl. Phys.* **1979**, *12*, L113.
- (7) Collins, R. L. Hydrogen Detector. General Electric Co., U.S. Patent 3,559,457, February 2, 1971.
- (8) Norton, F. J. Gas Analyzer. General Electric Co., U.S. Patent 2,307,800, January 12, 1943.

- (9) Shaver, P. J. *Rev. Sci. Instrum.* **1969**, *40*, 901.
- (10) Berlin, C. W.; Sarma, D. H. R. Thick Film Sense Resistor Composition and Method of Using the Same. Delco Electronics Corp., U.S. Patent 5,221,644, June 22, 1993.
- (11) DiMeo, F. J.; Chen, B. *Proc. 2000 DOE Program Rev.*; U.S. Department of Energy, 2000.
- (12) Hoffheins, B. S.; Lauf, R. J. Thick-Film Hydrogen Sensor. Martin Marietta Energy Systems, Inc., U.S. Patent 5,451,920, September 19, 1995.
- (13) Hoffheins, B. S.; Maxey, L. C.; Holmers, W. J.; Lauf, R. J.; Salter, C.; Walker, D. *Proc. 1999 DOE Hydrogen Program Rev.*; U.S. Department of Energy, 1999.
- (14) Lauf, R. J.; Hoffheins, B. S.; Fleming, P. H. Thin film hydrogen sensor. Martin Marietta Energy Systems, Inc., U.S. Patent 5,367,283, November 22, 1994.
- (15) Lauf, R. J.; Salter, C.; Smith, R. D. *J. Proc. 2000 DOE Hydrogen Program Rev.*; U.S. Department of Energy, 2000.
- (16) Bévenot, X.; Trouillet, A.; Veillas, C.; Gagnaire, H.; Clement, M. *Sens. Actuators B* **2000**, *67*, 57–67.
- (17) Butler, M. A. *Sens. Actuators B* **1994**, *22*, 155–163.
- (18) Garcia, J. A.; Mandelis, A. *Rev. Sci. Instrum.* **1996**, *67*, 3981.
- (19) Mandelis, A.; Garcia, J. A. *Sens. Actuators B* **1998**, *49*, 258–267.
- (20) Okuhara, Y.; Takata, M. *Bull. Mater. Sci.* **1999**, *22*, 85–87.
- (21) Sekimoto, S.; Nakagawa, H.; Okazaki, S.; Fukuda, K.; Asakura, S.; Shigemori, T.; Takahashi, S. *Sens. Actuators B* **2000**, *66*, 142–145.
- (22) Tobiska, P.; Hugon, O.; Trouillet, A.; Gagnaire, H. *Sens. Actuators B* **2001**, *74*, 168–172.
- (23) Dwivedi, D.; Dwivedi, R.; Srivastava, S. K. *Sens. Actuators B* **2000**, *71*, 161.
- (24) Formoso, M. A.; Maclay, G. J. *Sens. Actuators B* **1990**, *2*, 11.
- (25) Lundstrom, I. *Sens. Actuators* **1981**, 403.
- (26) Ruths, P. F.; Ashok, S.; Fonash, S. J.; Ruths, J. M. *IEEE Trans. Electron Devices* **1981**, *ED28*, 1003.
- (27) Shivaraman, M. S.; Lundstrom, I.; Svensson, C.; Hammarsten, H. *Electron. Lett.* **1976**, *12*, 484.

Scheme 1. (a) Schematic Diagram of a PMA-Based Hydrogen Sensor or Switch. (b) SEM Image of a PMA-Based Hydrogen Sensor



of dihydrogen, tends to be rate-limiting. In principle, then, by reducing the dimensions of the Pd sensing element, the time required for hydrogen atoms to diffusely equilibrate with this element can be reduced, and the response of the sensor to hydrogen gas can be accelerated. This strategy has already been used to achieve a response time of 400–500 ms for a heated Pd thin-film resistor-based sensor.<sup>11</sup>

In this paper, we have taken this strategy one step further by fabricating hydrogen sensors and hydrogen-actuated switches from arrays of mesoscopic Pd wires, as shown in Scheme 1.<sup>29</sup> These resistance-based devices operate at room temperature, exhibit a response time to 10% H<sub>2</sub> in air as low as 20 ms, and consume less than 10<sup>-8</sup> W of power. The mechanism of sensor operation, however, is different from all existing Pd resistor-based H<sub>2</sub> sensors. Specifically, whereas conventional Pd resistor-based sensors become more resistive in the presence of hydrogen,<sup>10–15</sup> Pd mesowire arrays (PMAs) become more conductive.<sup>29</sup> This inverted response is the consequence of a unique mechanism of operation. In this paper, the performance and mechanism of operation for PMA H<sub>2</sub> sensors are examined in greater detail.

(28) Lewis, F. A. *The Palladium Hydrogen System*; Academic Press: New York, 1967.

(29) Favier, F.; Walter, E. C.; Zach, M. P.; Benter, T.; Penner, R. M. *Science* **2001**, *293*, 2227.

## EXPERIMENTAL SECTION

**Electrochemical Measurements.** All chemicals were reagent grade from Fisher and were used without further purification. Two different Pd plating solutions were used: aqueous 2 mM PdCl<sub>2</sub>, 0.1 M HCl and 2 mM Pd(NO<sub>3</sub>)<sub>2</sub>, 0.1 M HClO<sub>4</sub>. Barnstead Nanopure deionized water ( $\rho > 17.8 \text{ M}\Omega$ ) was employed for all solutions. Pd plating solutions were sparged for 10 min with prehumidified N<sub>2</sub> prior to use. Cyclic voltammograms (CVs) and potentiostatic metal plating pulses were applied using an EG&G model 263A potentiostat. All deposition experiments were carried out in a glass electrochemical cell. Highly oriented pyrolytic graphite was freshly cleaved with adhesive tape and held using a Teflon electrode holder. Approximately 0.3 cm<sup>2</sup> of this graphite sample was exposed to the Pd plating solution in the electrochemical cell. A saturated calomel reference electrode (SCE) was employed as the reference electrode. A platinum foil (~4 cm<sup>2</sup>) was employed as the counter electrode in all experiments.

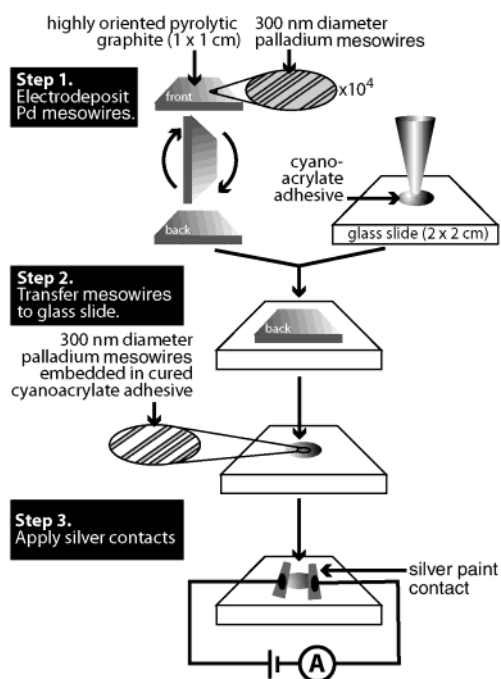
**Microscopy.** Samples to be examined using the scanning electron microscope (SEM) were mounted on an aluminum SEM stub using adhesive carbon dots (Ted Pella, Inc). Scanning electron microscopy was carried out using a Philips model XL-30FEG operating at 10 keV. Transmission electron microscopy (TEM) samples were prepared by mechanically transferring Pd mesowires to carbon-coated TEM grids (PELCO). Following deposition, the HOPG surface was rinsed with Nanopure water. TEM images were acquired using a Philips EM-200 operating at 200 keV. Selected area electron diffraction patterns were acquired using a camera length of 1.35 m and a 10- $\mu\text{m}$  aperture.

Atomic force microscope images were acquired on Pd mesowires on graphite using a Park Scientific Instruments Autoprobe cp operating in noncontact mode. Images in H<sub>2</sub> were acquired by exposing the sample to a stream of 10% H<sub>2</sub> in N<sub>2</sub> during image acquisition.

**Sensor Fabrication.** PMA hydrogen sensors such as that shown in Scheme 1 were prepared using the procedure shown in Scheme 2. Briefly, the surface of the graphite electrode onto which Pd mesowires had been deposited was pressed onto a droplet (~50  $\mu\text{L}$ ) of cyanoacrylate adhesive (Special T super glue, Satellite City) on a degreased glass slide. After this adhesive hardened, the graphite surface was lifted off the cyanoacrylate, and residual carbon layers were removed with a forceps. The vast majority of the mesowires initially present on the graphite surface were transferred onto the surface of the cyanoacrylate film using this procedure. With the aid of an optical microscope, silver contacts (conductive liquid silver, Ted Pella) were manually applied to the two ends of a mesowire array using a thin glass pipet. Macroscopic copper wires were also attached to these contacts to facilitate resistance measurements.

**Hydrogen Sensing.** Most sensor measurements were carried out in a sealed ~50-mL glass jar to which gas inlets and outlets had been attached. A MKS-type 647B mass flow and pressure programmer was used in conjunction with a MKS mass flow controller to produce a flow rate of 200 sccm ( $\pm 2$  sccm) in all gas flow measurements. The response time of this controller was <100 ms. Sensor response times were measured in a smaller-volume cell having a dead volume of ~1 mL, using gas flow rates of 200 sccm through a solenoid valve with a switching time of ~10 ms. Sensor currents were measured using a potenti-

Scheme 2. Procedure for Fabrication of H<sub>2</sub> Sensors Based on PMAs



stat (EG&G model 263A), which also provided a bias of 5 or 10 mV.

## RESULTS AND DISCUSSION

**Palladium Mesowire Growth.** The first step in the fabrication of PMA H<sub>2</sub> sensors involved the electrodeposition of Pd mesowires onto a highly oriented pyrolytic graphite (HOPG) surface. These mesowires nucleate and grow at defects on the graphite surface called step edges, and the length and shape of these mesowires is dictated by the corresponding length and topology of the step edges present on the graphite basal plane (i.e., the 0001 surface). Some pertinent information about these graphite surfaces is the following: The HOPG employed for this study is a polycrystalline material in which individual crystallites or grains have lateral dimensions of 50–500 μm. Within the confines of a particular grain and on the 0001 surface, the predominant defect is an incomplete graphite layer that, together with the graphite layers below it, forms a “step edge” having a height of between 3.3 Å (one graphite layer) to hundreds of angstroms (many graphite layers). On average, these step edges are approximately linear, are oriented approximately parallel to one another, and are separated from one another by between 500 and 5000 nm on the surface. Consequently, within a single 50–500-μm-diameter grain, there can be hundreds of step edges. Because individual steps are not continuous across grain boundaries, the length of the longest mesowires that can be produced by step edge decoration equals the grain diameter.

These step edges can be selectively decorated with metal oxides (e.g., MoO<sub>2</sub><sup>30</sup>) or metals (e.g., Pd<sup>29</sup>) electrochemically. The growth of the Pd mesowires required for PMAs can be understood with reference to Figure 1. In Figure 1a is shown a cyclic voltammogram for a solution containing aqueous 2 mM Pd<sup>2+</sup> and 0.1 M HCl at a freshly cleaved HOPG surface. As the potential of this electrode is scanned negatively from +0.8 V, no Pd deposition

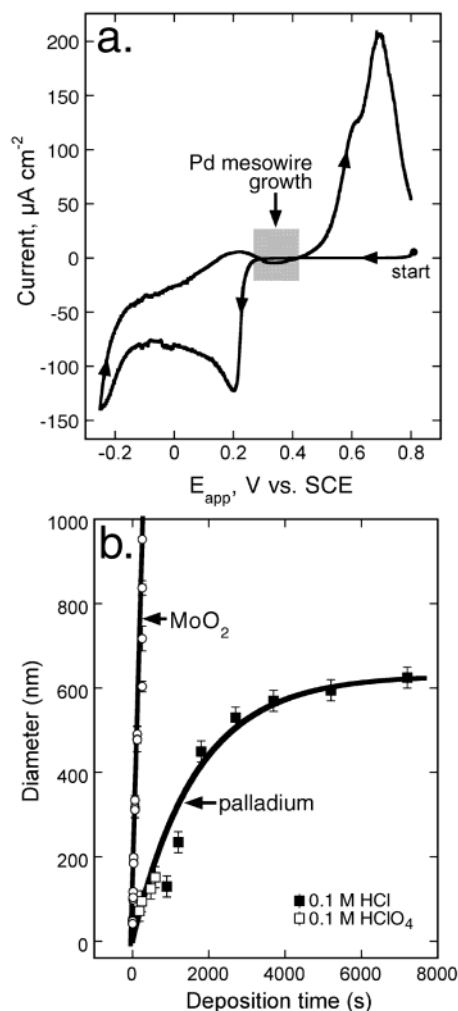


Figure 1. (a) Cyclic voltammogram at 20 mV s<sup>-1</sup> for an HOPG electrode in an aqueous Pd plating solution containing 2 mM Pd<sup>2+</sup>, 0.1 M HCl. The growth of Pd mesowires was accomplished using potentials in the gray region. (b) Plots of wire diameter versus deposition time for the deposition of MoO<sub>2</sub> mesowires (ref 29) and Pd mesowires. For Pd mesowires, data for depositions carried out both in HCl and HClO<sub>4</sub> electrolytes containing 2 mM Pd<sup>2+</sup> are shown.

current is seen until +0.20 V; 0.55 V negative of the reversible potential for Pd deposition. This suppression of plating current reveals the existence of an energetic barrier for the nucleation of Pd on clean HOPG. This barrier is somewhat lower at surface defects, such as step edges, than at atomically smooth terraces on this surface. This conclusion follows from the fact that at deposition potentials in the range from 0.25 to 0.4 V vs SCE (gray region, Figure 1a), the deposition of Pd occurs predominantly at step edges. Pd wires formed at this potential are discontinuous. Wires that are continuous and hundreds of microns in length can be formed by first pulsing the plating potential to -0.2 V for 5 ms and then growing the resulting Pd nuclei at potentials from 0.25 to 0.4 V.

Pd mesowires formed using this procedure are shown in the scanning electron micrographs of Figure 2. These mesowires were prepared using two different plating electrolytes: 2 mM Pd<sup>2+</sup>, 0.1 M HCl (Figure 2a,b) and 2 mM Pd<sup>2+</sup>, 0.1 M HClO<sub>4</sub> (Figure 2c,d). Mesowires produced from the chloride electrolyte had large grains 100 nm or more in diameter and a rough surface. The smallest wires obtainable from this plating solution were ~150 nm in

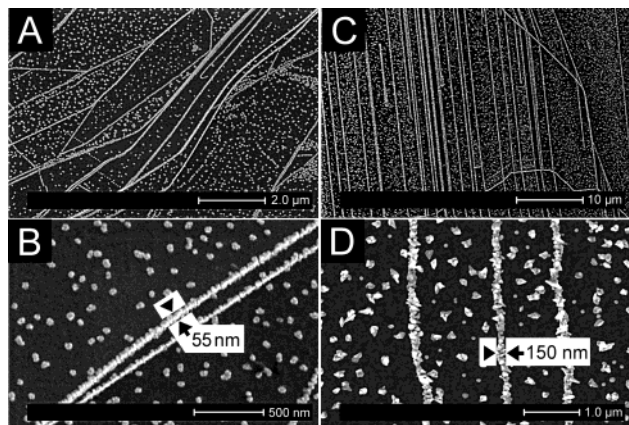


Figure 2. (A, B) Scanning electron micrographs (SEMs) of Pd mesowires prepared by electrodeposition from aqueous 2.0 mM Pd(NO<sub>3</sub>)<sub>2</sub>, 0.1 M HClO<sub>4</sub>,  $E_{\text{dep}} = 0.3$  V,  $t_{\text{dep}} = 150$  s; and (C, D) from aqueous 2.0 mM PdCl<sub>2</sub>, 0.1 M HCl,  $E_{\text{dep}} = 0.3$  V,  $t_{\text{dep}} = 900$  s.

diameter. A somewhat smoother morphology for mesowires was obtained in the perchlorate electrolyte, and this facilitated the growth of smaller mesowires down to 50 nm in diameter; however, mesowire arrays produced from these two solutions were indistinguishable in terms of their behavior in PMA H<sub>2</sub> sensors.

During mesowire growth, a constant deposition current ranging from 20 to 80  $\mu\text{A cm}^{-2}$  was observed (data not shown). If this current is associated purely with the deposition of hemicylindrical mesostructures, the radius of these structures,  $r(t)$ , increases according to<sup>30</sup>

$$r(t) = \sqrt{\frac{2i_{\text{dep}}t_{\text{dep}}V_{\text{m}}}{\pi nFl}} \quad (1)$$

where  $V_{\text{m}}$  is the molar volume of metal (8.86 cm<sup>3</sup> mol<sup>-1</sup> for Pd),  $n$  is the number of electrons transferred for the deposition of each metal atom, and  $l$  is the total length of mesowires on the graphite surface. In fact, eq 1 is not obeyed for the growth of Pd mesowires, possibly because a significant number of particles nucleate and grow in parallel with the wires on the graphite surface (vide infra), and the growth law for these particles is  $r(t) \propto t^{1/3}$ .<sup>31</sup> However, as shown in the plot of Figure 1b, the diameter of Pd mesowires increases smoothly with deposition time over the range from 50 to 600 nm. A key point, shown in Figure 1b, is that the rate of growth for Pd mesowires is much slower than we have reported for the growth of MoO<sub>2</sub> mesowires.<sup>30</sup> Pd mesowires grow more slowly because of the smaller  $V_{\text{m}}$  for Pd (19.8 cm<sup>3</sup> mol<sup>-1</sup> for MoO<sub>2</sub> vs 8.86 cm<sup>3</sup> mol<sup>-1</sup> for Pd) and because a smaller overpotential was employed for wire growth. We found that this slower growth rate was essential in order to obtain preferential growth of Pd wires at steps.

**Evaluation of Sensor Performance.** PMAs were operated as gas sensors by applying a voltage bias of either 5 or 10 mV across the array and measuring the current using a conventional potentiostat. Typical data for several pure gases are shown in Figure 3. Exposure to hydrogen caused a prompt increase in the current through the device, whereas exposure to other gases (O<sub>2</sub>, saturated H<sub>2</sub>O in N<sub>2</sub>, Ar, and He) did not measurably affect the

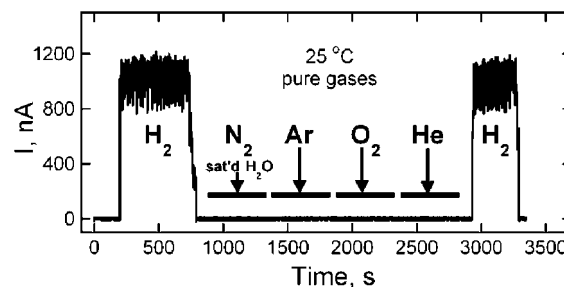


Figure 3. Response of a mode II PMA sensor to four pure gases and humid nitrogen. Sensor bias, 5 mV.

resistivity. The decreased resistance of PMAs in the presence of hydrogen is exactly the opposite of the response of conventional resistance-based sensors constructed using Pd films.<sup>10–15</sup> The resistivity of PdH<sub>x</sub> is increased by a factor of 1.8 as hydrogen is absorbed and  $x$  increases from 0 to 0.7 (saturation in 1 atm H<sub>2</sub> at 25 °C).<sup>28</sup> The resistance of macroscopic Pd resistors, therefore, increases by 1.8 in the presence of pure hydrogen. In the absence of hydrogen, the sensor evaluated in Figure 3 reverted to open circuit (i.e., a total resistance of > 30 M $\Omega$ ). We discuss the unique mechanism of PMA sensor operation in detail later.

The fabrication procedure shown in Scheme 2 produced H<sub>2</sub> sensors of two types: Approximately 90% of PMAs reverted to an open circuit condition in the absence of hydrogen, as shown in Figure 3. These hydrogen-actuated switches were termed “mode II” sensors. The remaining 10% of the PMAs exhibited a lower but nonzero resistance in the absence of hydrogen. These we termed “mode I” sensors. Plots of  $i_{\text{sensor}}$  vs time for a range of H<sub>2</sub> concentrations are shown in Figure 4a,b for both types of sensors. Mode I sensors typically had a limit of detection of 0.5% H<sub>2</sub>, and mode II sensors typically “switched on” at 2% H<sub>2</sub>. However both types of sensors exhibited sigmoidal current versus [H<sub>2</sub>] response characteristics, shown in Figure 4c.

On the basis of the arguments advanced in the Introduction, we expected PMA-based hydrogen sensors to respond more rapidly to hydrogen than existing sensors based on palladium films. This expectation is realized for relatively high concentrations of H<sub>2</sub> of >8%, for which we observe a time response in the 20–50 ms range (e.g., Figure 5a). However, as shown in Figure 5b, at lower H<sub>2</sub> concentrations in the 2–6% range, PMA sensors exhibited a much slower response in the range from 2 to 5 s. Surprisingly, at still lower [H<sub>2</sub>] concentrations below 2%, the sensor response time again become <1 s. This complex behavior is not explained by a simple diffusion-limited sensor response, and more experimentation will be needed in order to elucidate its origin. It is worth noting, however, that there are literature precedents for H<sub>2</sub> sensor responses that are slower than expected on the basis of the diffusion distance for H atoms in the palladium sensor element. Bévenot et al.,<sup>16</sup> for example, recently reported an evaluation of an optical sensor based on a 13-nm-thick palladium film that exhibits a response time of 1 to 100 s.

A final point is that the resistance change seen for PMA sensors was much larger than is possible for conventional palladium resistors. The sensor evaluated for Figure 4a, for example, had a baseline resistance ( $R_0$ ) that was a factor of 4 greater than the resistance in 10% H<sub>2</sub>. As already indicated above, an increase in  $R/R_0$  of 1.8 is the maximum normally seen for conventional palladium resistors. Thus, both the magnitude of the

(30) Zach, M. P.; Ng, K.; Penner, R. M. *Science* **2000**, *290*, 2120.

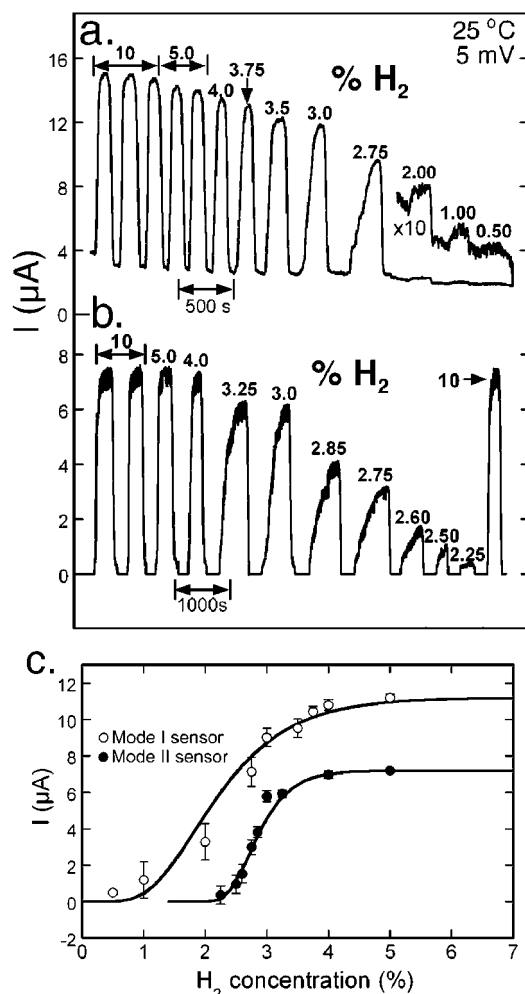


Figure 4. (a) Current response of a mode I sensor to hydrogen/nitrogen mixtures (concentration of  $H_2$  in %, as shown). Data were acquired in random order of  $H_2$  concentration. (b) Current response of a mode II sensor to hydrogen/nitrogen mixtures (concentration of  $H_2$  in %, as shown). Data were acquired in random order of  $H_2$  concentration. (c) Current amplitude versus  $H_2$  concentration for these same two sensors.

resistance change and its sign were distinctly different from what is normally observed for resistive  $H_2$  sensors. The unusual mechanism of response responsible for these characteristics is discussed next.

**Mechanism of Sensor Function.** PMA sensors operate by a fundamentally different mechanism from all other resistance-based hydrogen sensors. To elucidate this mechanism, we first examined functioning PMA sensors using SEM. A specimen was prepared for imaging by coating a functional sensor with a thin layer of gold/palladium alloy. A sequence of 15 SEM images spanning the entire width of the sensor gap are shown at the top of Figure 6, and below it, the right side of this gap is shown at higher magnification. These images clearly show that the Pd mesowires in the sensor are discontinuous. Multiple breaks, with widths of 40–80 nm and spaced by 2–5  $\mu\text{m}$ , are seen in each mesowire in the sensor. For one Pd mesowire in Figure 6, these breaks are labeled “b”. Also labeled are two other features commonly seen in SEMs: segments of mesowire where the wire becomes submerged in the cyanoacrylate (“s”), and terminations (“t”) where a mesowire ended prior to making contact with the silver

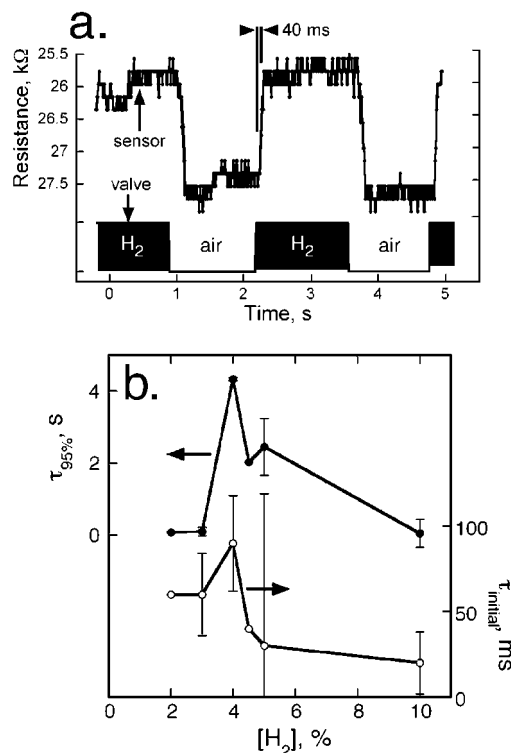


Figure 5. (a) Sensor resistance versus time response for a mode I sensor. This is the only experiment of those shown in this paper for which the gas transport system was optimized for fast time response. (b) Response time as a function of  $[H_2]$ . Both the initial response time,  $\tau_{\text{initial}}$ , defined as the increase in sensor signal above background ( $\bullet$ ), and the “95%” response time,  $\tau_{95\%}$ , defined as the time required for the sensor to produce 95% of the output observed at long times ( $\circ$ ), are plotted.

current collector. It is the breaks in these mesowires, however, that form the basis for sensor function.

The nanoscopic breaks in each mesowire function as break junctions that close in the presence of hydrogen, and open in its absence. The reversible cycling of one such break junction is shown in a sequence of atomic force micrographs shown in Figure 7. At top is shown a freshly deposited Pd mesowire on a graphite surface. The diameter of this wire as estimated from its height above the graphite surface was 200 nm. Within the white circle at left is a gap with an apparent width of 50 nm. The next AFM image in the sequence was acquired while the mesowire was exposed to  $\sim 1$  atm  $H_2$  gas. The height of the mesowire in this image is increased by 2–12%, and the gap present in air has closed. Subsequent air/ $H_2$  cycles (third and fourth images) caused this break junction to reopen and reclose. This experiment demonstrates that reversible opening and closing of nanobreak junctions can occur, at least for mesowires located on a graphite surface. We assume that these break junctions also open and close reversibly after embedding in the cyanoacrylate film, but we have not yet been able to observe break junctions in operating  $H_2$  sensors using AFM.

As-deposited palladium mesowires do not contain breaks. How, then, are these break junctions formed? One possibility is that break junctions are formed during the embedding and transfer process. Arguing against this is the fact that the spacing between breaks, and the break widths themselves, are both narrowly distributed about a mean value. A second possibility is that  $H_2$

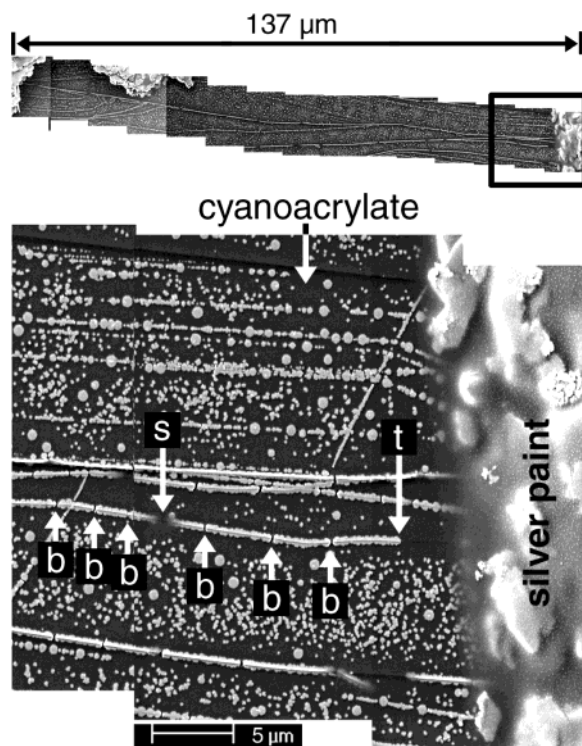


Figure 6. SEM images of a PMA-based  $H_2$  sensor that functioned for several weeks. At top is shown an ensemble of 15 images that span a section of the  $140\text{-}\mu\text{m}$  sensor gap. Below, three images show the topology of the Pd structures in greater detail. Three types of defect structures are indicated: break junctions (b), a subsurface traverse of a mesowire into the cyanoacrylate (s), and a mesowire termination (t).

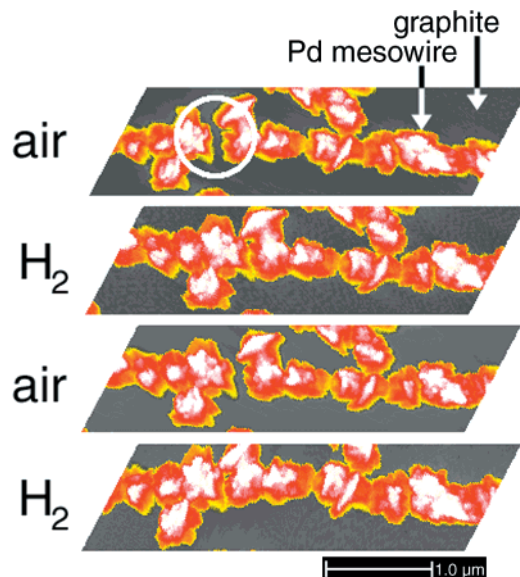


Figure 7. Atomic force microscope images of a Pd mesowire on a graphite surface. These images were acquired either in air or in a stream of  $H_2$  gas, as indicated. A hydrogen-actuated break junction is highlighted (circle).

exposure causes break junction formation. We tested this hypothesis by investigating the structure of freshly deposited Pd mesowires on the graphite surface by SEM before embedding and transfer. These mesowires were then reimaged on the graphite surface after 5, 10, 20, 50, and 100 air/ $H_2$ /air cycles. Typical results for one mesowire are shown in Figure 8. At the

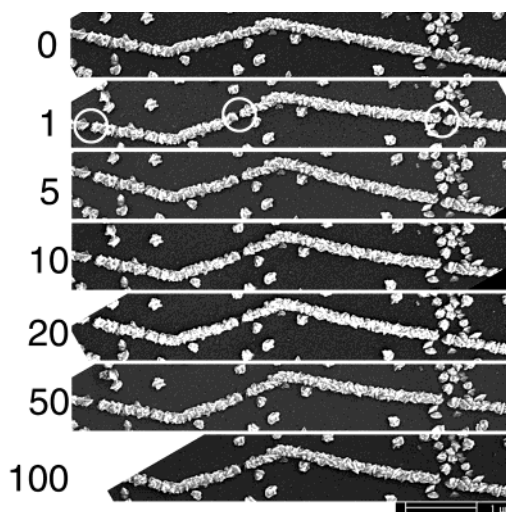


Figure 8. Series of SEM images of the same Pd mesowire. The mesowires present on this surface were subjected to multiple air/ $H_2$ /air cycles. The number of cycles is indicated at left.

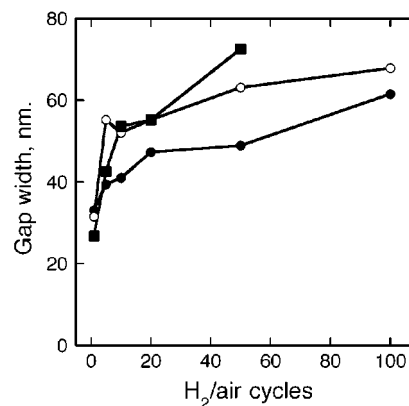


Figure 9. Plot of break width as a function of the number of air/ $H_2$ /air cycles for the three break junctions shown in Figure 8.

top of this figure is shown a freshly deposited Pd mesowire in which no breaks are observed. The first  $H_2$ /air cycle (second image) opened three breaks, as indicated. These breaks had widths of 25–35 nm (Figure 9). After 20–50  $H_2$ /air cycles, the widths of these breaks grew by a factor of 2, but no new breaks were formed. Further increases in the widths of these breaks after 100  $H_2$ /air cycles were small. A second important observation is that the microtopography of the Pd mesowire and of the surrounding Pd particles is not altered, even after 100  $H_2$ /air cycles, except for the formation of break junctions. It has been known for many years<sup>28</sup> that exposure of Pd metal to multiple  $H_2$ /air cycles induces profound morphological changes, including changes to the macroscopic dimensions of Pd metal pieces. On a microscopic scale, the formation of parallel slip bands has been reported. These topological changes are the result of plastic deformation of the metal lattice driven by the strain caused by the  $\alpha$ -to- $\beta$ -phase transition.<sup>28</sup> The microscopic dimensions of the palladium grains in our mesoscale structures must be a factor in the elastic accommodation of this strain by the Pd.

On the basis of the result of Figure 8, we predict that the resistance of a freshly prepared PMA sensor *in air* should increase dramatically after one  $H_2$ /air cycle because of the introduction of break junctions into each mesowire in the sensor. As shown in

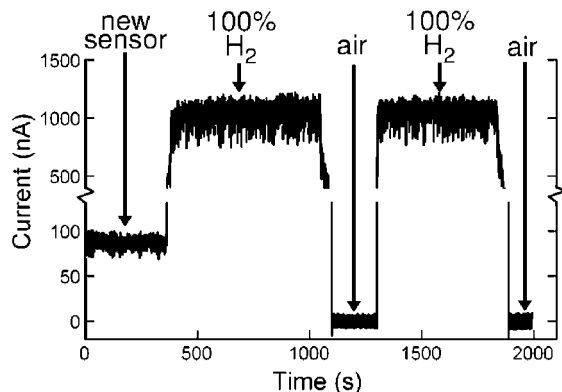


Figure 10. Plot of sensor current versus time for the first exposure of a new sensor to hydrogen and one subsequent H<sub>2</sub>/air cycle. This sensor exhibited a mode II response.

### Scheme 3. Proposed Mechanism of Nanobreak Junction Formation and Sensor Function

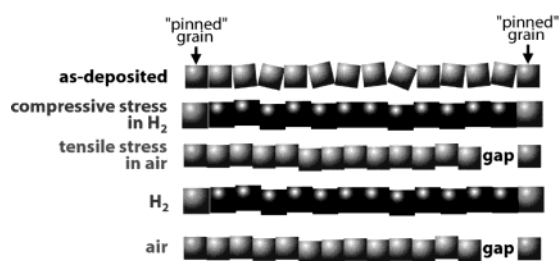
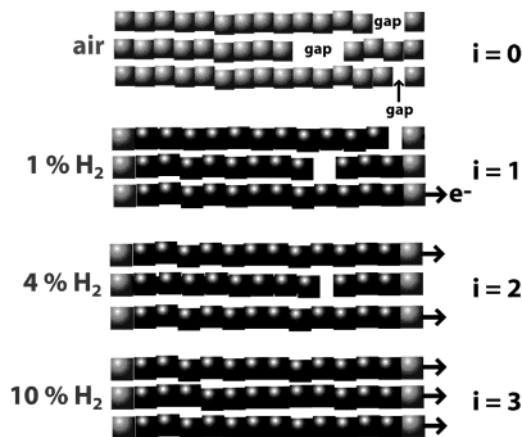


Figure 10, this is typically what was observed. Here is plotted the sensor current during the first exposure to 100% H<sub>2</sub> and transfer to air. In this particular case, transfer from H<sub>2</sub> to air caused the sensor current to decrease to near zero, indicating the formation of a mode II device. Although as-deposited Pd mesowires did not contain break junctions, an *increase* in the sensor current is observed when a freshly prepared sensor is exposed to H<sub>2</sub> for the first time. This is despite the fact that the resistivity of individual Pd grains in each mesowire must increase by a factor of 1.8 during after absorbing H<sub>2</sub>! Our explanation for this unexpected effect is presented below.

Collectively, the data presented above are consistent with the mechanism for sensor formation shown in Scheme 3. This mechanism can be summarized as follows: Freshly deposited polycrystalline Pd mesowires are electrically continuous and exhibit a resistance that is concentrated at grain boundaries. The first exposure of these wire to H<sub>2</sub> at a concentration above 0.8% at 298 K induces a phase transition from  $\alpha$  to  $\beta$  and the expansion of the face-centered cubic (fcc) Pd lattice by 3.5%.<sup>28</sup> This lattice expansion is accommodated by a 3.5% compression of each mesowire along its axis; this compression occurs preferentially at grain boundaries and results in the lowering of the intergranular resistance and an increased conductance for each mesowire. The decreased intergranular resistance must be larger than the increased resistance of each grain associated with the formation of the palladium hydride, because if this were not the case, the overall sensor current would decrease instead of increase upon exposure to H<sub>2</sub> for the first time. Removal of the mesowires to a pure air ambient induces a  $\beta$ -to- $\alpha$ -phase transition, the contraction of each grain by 3.5%, and the application of a tensile stress to each mesowire that is relieved by the opening of nanoscopic

### Scheme 4. Proposed Mechanism for the Increase in Sensor Conductivity with Increasing H<sub>2</sub> Concentration



breaks. Subsequently, the compressive and tensile stress associated with reversible H<sub>2</sub> absorption is accommodated by the opening and closing of these break junctions.

The proposed mechanism by which the H<sub>2</sub> concentration-dependent sensor response seen in Figure 4 is produced is shown in Scheme 4. This mechanism can be summarized as follows: Every mesowire in a sensor functions as a switch. At a threshold concentration of H<sub>2</sub> that is different for every mesowire, all of the breaks in a mesowire close, and a new channel for conduction across the sensor gap is opened. The H<sub>2</sub> concentration-dependent sensor current,  $i_{\text{sensor}}$ , is the sum of the currents through each of these mesowires.

$$i_{\text{sensor}}([\text{H}_2]) = V \sum_{i=1}^{n_c([\text{H}_2])} \frac{1}{R_i} \quad (2)$$

where  $V$  is the applied bias,  $n_c$  is the number of conductive mesowires, and  $R_i$  is the resistance of each. On the basis of eq 2, the sensor response function depends only on  $n_c([\text{H}_2])$  if  $R$  can be considered to be approximately the same for all mesowires. Thus, it is useful to ask whether the sigmoidal behavior for  $n_c([\text{H}_2])$  seen in Figure 4c is expected. We arrive at an answer by considering a single mesowire with  $N$  break junctions. Let us assume that as the H<sub>2</sub> concentration is increased from zero, these break junctions are characterized by a critical concentration of H<sub>2</sub> for which the closing of the junction is most probable. If this is the case, the probability,  $P(\text{H}_2)$ , that any one break junction will be closed is simply the integral of this Gaussian (Figure 11,  $N=1$ ). If a mesowire contains two break junctions, the probability that both are closed (and that the wire is conductive) will be  $P^2$ , and for  $N$  junctions,  $P^N$ . If it can be assumed that the many mesowires present in a sensor are similar, a plot of  $P^N$  provides an estimate of the normalized sensor response (sensor current,  $I_{\text{sensor}}$ , normalized by the saturation current measured at high [H<sub>2</sub>],  $I_s$ ). As seen in Figure 11, these plots are sigmoidal, and for values of  $N > 1$ , these response curves are shifted to higher concentrations from [H<sub>2</sub>]<sub>c</sub>. In principle, then, the number of break junctions, which can be controlled via the sensor gap width, provides a means by which the range of sensor sensitivity to hydrogen can be adjusted and the limit of detection for H<sub>2</sub> can be extended.

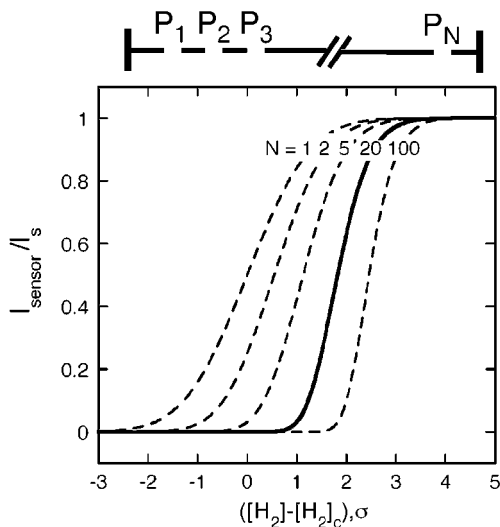


Figure 11. Calculation of the normalized sensor response as a function of the  $\text{H}_2$  concentration measured as the deviation from  $[\text{H}_2]_c$  in units of the standard deviation of  $[\text{H}_2]$  from  $[\text{H}_2]_c$ .  $N$  is the number of break junctions present in the mesowire. The response curve for  $N = 20$ , the typical number of break junctions present in functioning sensors, is highlighted.

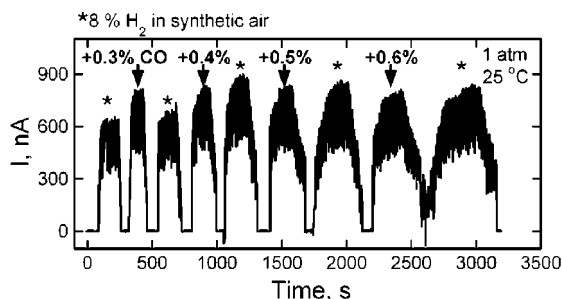


Figure 12. Response of a mode II PMA sensor to 8%  $\text{H}_2$  in synthetic air with and without added CO, as indicated.

**Sensor Performance in CO.** PMA  $\text{H}_2$  sensors did not register any response to  $\text{H}_2\text{O}$ ,  $\text{O}_2$ , or methane, and exposure to these reactive gases did not affect sensor performance for  $\text{H}_2$ . Especially in the case of  $\text{O}_2$ , this is a significant result, since  $\text{O}_2$  acts to inhibit the incorporation of H into Pd both by blocking incipient adsorption sites and by combining with chemisorbed H to produce water.<sup>32</sup>

Carbon monoxide adversely affects palladium-based sensors by chemisorbing to the palladium surface and blocking incipient adsorption sites for  $\text{H}_2$ . It is typical for the response time of  $\text{H}_2$  sensors to increase by a factor of 2–10 upon exposure to small concentrations of CO (20–50 ppm). In one recent study,<sup>33</sup> the response time for 2%  $\text{H}_2$  increased from 1 to 4 min after exposure to 25 ppm CO. The original response time was recovered after exposure of the sensor to air for several minutes. The results of an experiment involving exposure of a PMA sensor to high concentrations of CO above 3000 ppm is shown in Figure 12. In this experiment, the response of a PMA sensor to 8%  $\text{H}_2$  in synthetic air was evaluated with and without added CO at concentrations between 3000 and 6000 ppm.

Two aspects of this experiment are notable. First, the addition of CO at high concentrations does not interfere with the detection of 8%  $\text{H}_2$ , and even the response time is not adversely affected initially. In fact, the presence of 3000 ppm CO increases in the amplitude of the sensor current by 5–10%, perhaps by removing physisorbed  $\text{O}_2$  as  $\text{CO}_2$  from the palladium surface, as previously reported.<sup>32</sup> With subsequent exposures to CO at concentrations up to 6000 ppm, the response time of this sensor is progressively slowed to a maximum of several minutes. Exposure of this sensor to air resulted in a complete recovery of the original temporal response in a few minutes (data not shown). The relative immunity exhibited by PMA sensors to CO poisoning may derive from the higher surface-area-to-volume ratio of Pd mesowires relative to Pd films used in most conventional sensors. A qualitative explanation is as follows: After exposure of a palladium surface to CO, a small number of “pinholes” of clean palladium are likely to remain in a monolayer of chemisorbed CO. These pinholes provide a small number of sites for the dissociation of  $\text{H}_2$ . If this sensor is exposed to hydrogen, the flux of protons into a palladium sensor element through these pinholes will be much slower than for a clean palladium surface. The impact of this reduced reaction rate for dihydrogen at the palladium surface depends on the volume of palladium metal that must be equilibrated with atomic hydrogen. If the volume of palladium is small relative to the surface area, then equilibrium will be rapidly achieved, and sensor response will be minimally impacted. This is what may be occurring in the case of PMA hydrogen sensors.

## SUMMARY

Long, mesoscopic noble metal wires prepared by electrodeposition offer new opportunities for the construction of sensors. In this paper, the fabrication of a new type of hydrogen sensor based on arrays of palladium wires has been described. These sensors function by a novel mechanism involving the closing of many nanoscopic break junctions in each wire upon exposure to  $\text{H}_2$ . Even though each Pd wire in these sensors is a two-state switch (i.e., conductive or insulating), the statistics of this transition for many mesowires imparts a  $\text{H}_2$  concentration dependence to the sensor conductivity. The break junctions that are essential for sensor function are themselves formed during the first exposure of the palladium wires to hydrogen.

PMA-based  $\text{H}_2$  sensors offer the following several advantages when compared with existing  $\text{H}_2$  sensors: faster response times below 100 ms (for 8%  $\text{H}_2$ ); improved performance in the presence of high concentration of reactive gases including  $\text{O}_2$ ,  $\text{H}_2\text{O}$ ,  $\text{CH}_4$ , and CO; room temperature operation; and minute power requirements of a few nanowatts or less.

## ACKNOWLEDGMENT

This work was funded by the NSF (grant CHE-0111557) and the Petroleum Research Fund of the American Chemical Society (grant 33751-AC5). R.M.P. acknowledges the financial support of the A.P. Sloan Foundation Fellowship, and the Camille and Henry Dreyfus Foundation. F.F. acknowledges funding through NATO. Finally, donations of graphite by Dr. Art Moore of Advanced Ceramics are gratefully acknowledged.

Received for review September 28, 2001. Accepted January 7, 2002.

AC0110449

(31) Liu, H.; Penner, R. M. *J. Phys. Chem. B* **2000**, *104*, 9131–9139.

(32) Amandusson, H.; Ekedahl, L. G.; Dannetun, H. *Appl. Surf. Sci.* **2000**, *153*, 259–267.

(33) Pitts, J. R.; Liu, P.; Lee, S.-H.; Tracy, C. E.; Smith, R. D.; Salter, C. *Proc. 2000 DOE Hydrogen Program Rev.*; 2000.